Unraveling the Facet-dependent Surface Chemistry at Molecular Scale: Photo-assisted Oxidation of InP Nanocrystals

Eunhye Cho, Meeree Kim, Liyan Ouyang, Hyoin Kim, Guillaume Bonifas, Yannick Coppel, Céline Nayral, Fabien Delpech, Sohee Jeong

Unraveling the Facet-dependent Surface Chemistry at Molecular Scale: Photo-assisted Oxidation of InP Nanocrystals

Eunhye Cho, [†, #] Meeree Kim, [†, #] Liyan Ouyang, [§] Hyoin Kim, [†] Guillaume Bonifas, [§] Yannick Coppel, [□] Céline Nayral, [§] Fabien Delpech, [*, §] and Sohee Jeong [*, †, ‡]

[†]Department of Energy Science (DOES), Sungkyunkwan University (SKKU), Suwon 16419, Republic of Korea

[§]Laboratoire de Physique et Chimie des Nano-Objets (LPCNO), Université de Toulouse, CNRS, INSA, UPS, 31077 Toulouse Cedex 4, France

[□]Laboratoire de Chimie de Coordination, CNRS, UPR 8241, Université de Toulouse, 31077 Toulouse, France

[‡]Sungkyunkwan Institute of Energy Science and Technology (SIEST), Suwon 16419, Republic of Korea

Facet-dependent surface chemistry, Nuclear magnetic resonance spectroscopy, Oxidation, Indium phosphide, Semiconductor nanocrystals

ABSTRACT: The facet-dependent surface chemistry of nanocrystals (NCs) provides fundamental insights into chemical reactivities, which are critical to obtaining precise control over the NC surface. In this study, by obtaining InP NCs with well-defined {111} and {110}/{-1-1-1} facets (tetrahedron and tetrapods, respectively) capped with chloride-oleylamine ligands, the previously under-investigated facet-dependent surface chemistry of III-V materials is explored. Solid-state and solution NMR analyses show that InP tetrahedrons, with their single facet composition and stronger Lewis acidity, exhibit narrow ^{31}P and ^{115}In resonances as well as deshielded ^{13}C signals of α-carbon adjacent to the NH_2 group of oleylamine. As a result, InP tetrahedrons exhibit strong ligand binding and a notable presence of less-mobile oleylamine ligands on the surface, leading to the efficient blocking of access to external species. This is also consistent with the minimal blue-shift of 1st excitonic peak in absorption spectra and the strong resistance to photo-assisted surface oxidation of InP tetrahedrons. Our findings, supported by solid-state/solution NMR, FTIR, and XPS analyses, highlight the significance of facet-dependent reactivities to surface ligands, and thus, atmospheric moieties, enhancing the potential of III-V NCs in various optoelectronic applications.

INTRODUCTION

Over the last three decades, colloidal semiconductor nanocrystals (NCs) have served as new building blocks in a variety of applications, whose photophysical properties can be modulated by their size, shape, and compositions.[1-3] The surface of colloidal NCs is bound with ligand molecules, which influence the complementary properties of NCs by trap state passivation,[4-6] surface dipole change,[7-9] and blocking or accelerating the access of external molecules, *etc*.[10,11,31] Alongside advances in synthetic strategies for designing the core NCs, large efforts have been made to achieve precise control over the surface to enhance the NC properties.[12-17]

The precise control of the ligand-NC surface interactions poses a challenge mainly due to the complex reactivity of the multiple binding sites across the entire NC surface.[18] Accordingly, recent progress has strategically combined well-defined NCs with surface reactions as probing tools to advance the understanding and manipulation of surface chemistry.[19-21] One crucial strategy in this regard is facet-dependent chemistry. By simplifying the surface models into well-defined facets, the different reactivities towards foreign environments can be conjectured as considering the composition and arrangement of cationic/anionic sites on each facet. Thus, by scrutinizing the interplay between the NC surface and the reaction with external species, developing suitable passivation strategies for both polar and nonpolar surfaces and insights into the underlying mechanisms can be discerned.[22-24] Such insights for facet-dependent surface chemistry facilitate the development of NC-based devices for various applications.[25-30]

While this approach has been successfully extended to a diverse range of materials, including II-VI and IV-VI compounds, there has been a lack of comprehensive understanding of the true picture of the NC surface, particularly when III-V NCs are discussed. This is largely due to the lack of synthetic strategies to obtain well-defined NCs in III-V materials: the limited choice of available precursors and their covalent characteristics yielding high synthetic temperatures lead to uncontrolled reaction pathways. Nevertheless, the distinctive shape preference of InP NCs yielding {111}-terminated tetrahedral or {110}/{-1-1-1}-terminated tetrapodal geometry have been reported when halide-amine ligands are co-passivated without using the common acid ligands

affecting P elements of high oxophilicity.[32, 33] However, the physicochemical nature of their facet is still not straightforward, as each study largely relies on the uncontrolled or ill-defined variables introduced during the synthesis (or surface reactions), which leads to the surface structure uncertainty.

To this extent, herein, we have introduced two NCs with well-defined facets, being capped with the same surface ligand combination, and explored their facet-dependent surface chemistry. By avoiding the use of oxygen-containing molecules and modifying our previous synthetic strategy, two different types of oxide-free faceted NCs are obtained: chloride-oleylamine co-passivated NCs terminated by {111} facets and those terminated by {110}/{-1-1-1} facets. Given that In-rich {111} facets are polar and Lewis-acidic and the nonpolar {110} facets, consisting alternating In and P atoms, are less Lewis-acidic, their different reactivities towards external molecules are expected. Taking advantage of the nuclear magnetic resonance (NMR) studies, which have traditionally been used to gain molecular-level information by chemists, inorganic NC surface and the organic ligand molecules have been separately investigated. Throughout this comprehensive study, we aim to demonstrate the facet-dependent reactivities, particularly to surface ligands, for developing more efficient and demanding properties of semiconductor NCs. By advancing our understanding of these reactivities in relation to the photo-assisted oxidation reaction, this work could help to establish the chemical/structural strategies to achieve robust NCs, which are crucial for effectively manipulating NCs in solid-state optoelectronic devices within ambient environments. Although this approach does not entirely eliminate the complexity of intrinsic surface inhomogeneity (such as edge/vertex contributions and structural defects), it would provide complementary insights that contribute to mastering NC surface chemistry, an area that remains incompletely understood.

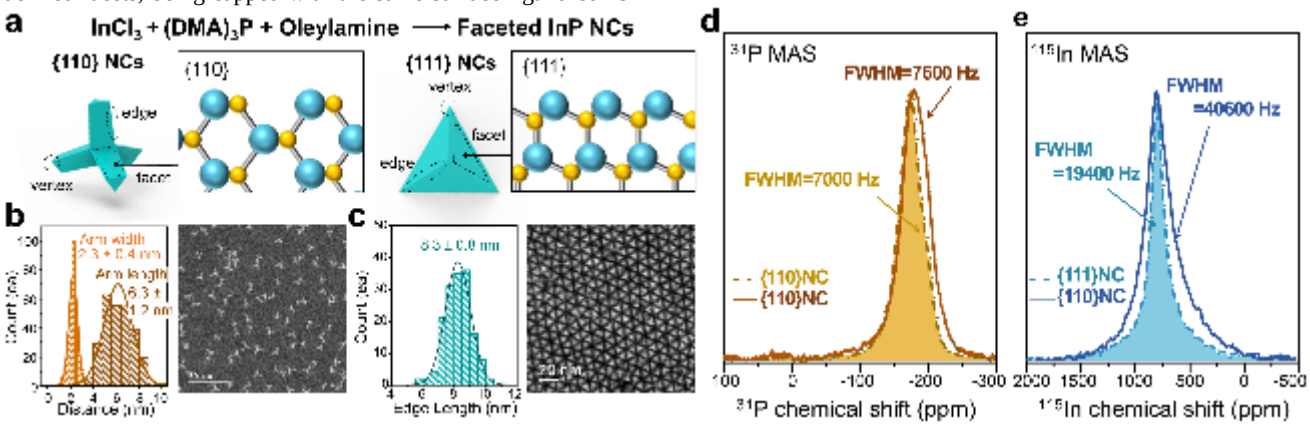

Figure 1. Synthesis and characterization of inorganic core for {111} and {110} InP NCs *via* MAS NMR spectroscopy. (a) Synthesis scheme for faceted InP NCs and their illustrations showing tetrapodal and tetrahedral geometry of {110} and {111} NCs, respectively. The side view of bare surface configuration of {110} and {111} facets are shown. Light blue and yellow atoms indicate indium and phosphorus, respectively. (b) STEM image (right) and size distribution histograms (left) for {110} NCs and (c) for {111} NCs. (d) $^{31}P\{^{1}H\}$ MAS NMR spectra for {110} NCs (solid line) and {111} NCs (dash-dotted line). (e) Static ^{115}In NMR spectra for {110} NCs (solid line) and {111} NCs (dash-dotted line).

RESULTS AND DISCUSSION

Characterization of inorganic core of {111} and {110} InP NCs

To investigate the surface nature of faceted InP NCs, we synthesized and purified two types of InP nanocrystals under an inert atmosphere following the method previously reported by Kim *et al.*[31]: Two types of zinc-blende InP NCs with different shapes and thus, with different facets exposed to the ligand were prepared[31] (Figure 1a and S2). Those displaying tetrahedral shape possess solely {111}-oriented surface and are referred to as {111} NCs (Figure 1a and S1a). The second type, exhibiting a tetrapod geometry predominantly covered with {110} surfaces and the minor facets being {-1-1-1} surfaces, is referred to as {110} NCs (Figure 1b and S1b). The scanning transmission electron microscopy (STEM) images show their sizes and size distributions: {110} NCs have 6.3 nm of arm length and 2.3 nm of arm width, while {111} NCs have 8.3 nm of edge length, respectively (Figure 1b and c).

In order to gain a better understanding and to provide a complete overview of the surface environment and chemistry of the {110} and {111} NCs, we have undertaken a full characterization of these samples using a combination of spectroscopic techniques (Fourier transform Infrared (FTIR) spectroscopy, synchrotron X-ray photoelectron spectroscopy (XPS) and solution and solid-state ^{1}H, ^{13}C, ^{31}P and ^{115}In NMR). The solvodynamic diameters of the {110} and {111} NCs (10.2 nm and 11.9 nm respectively for the {110} and {111} NCs) were determined by DOSY experiments and are consistent with the sizes estimated by TEM plus that of a layer of oleylamine ligands on the surface.[22] Magic angle spinning (MAS) NMR and XPS are particularly well-suited tools to characterize the inorganic core of InP NCs. $^{31}P\{^{1}H\}$ MAS NMR spectra of {110} and {111} NCs stored in inert atmosphere without exposure to ambient are presented in Figure 1d: the exclusive presence of resonances at -182 ppm and -174 ppm attributed to ^{31}P-In for {110} and {111} NCs, respectively, suggests their oxide free surfaces. These data are further supported by the XPS spectra (Figure S3 and S4), which show the absence of surface oxidation and other impurities for both {110} and {111} InP NC cores. Since the oxidation (formation of phosphate and indium oxide at the surface of InP NCs) would have resulted, on the one hand, in the appearance of resonances between 10 and -10 ppm in ^{31}P NMR[32] and the peak from 136 eV to 132 eV in P 2p core XPS spectrum for the phosphorus features,[33] and on the other hand, in the broadening of the In 3d XPS, the observed features are characteristics of the non-oxidized chemical environment. Static ^{115}In NMR spectra of {110} and {111} NCs stored in an inert atmosphere without exposure to air are also presented in Figure 1e showing resonances at 800 ppm and 788 ppm for {110} and {111} NCs, respectively.

Interestingly, despite both NCs being composed of identical components (*e.g.*, oxide-free InP cores with chlorine and oleylamine

surface ligands), {111} and {110} InP NCs can be distinguished in their NMR spectra (Figure 1d and 1e) by the linewidth of their resonance line shapes. When comparing ^{31}P and ^{115}In resonances of {111} and {110} InP NCs, it can be clearly seen that {110} NCs display broader signals. For the ^{115}In nucleus, the full width at half maximum (FWHM) of {111} and {110} InP NCs resonances are 19400 Hz and 40600 Hz respectively. For the ^{31}P phosphide resonances, the same trend is observed with a 10% broadening (from 7000 Hz to 7600 Hz). This difference can be explained by the variation in chemical environments of the surface In and P atoms in two NCs: The intrinsic surface inhomogeneity, such as facet distributions and edge/vertex contributions resulting from the NC geometry, distinguishes the two NCs. {110} NCs have a wider variety of surface chemical environments due to the presence of two different {110} and {-1-1-1} surfaces and the higher number of edges/vertices, while {111} NCs mainly consist of {111} facets

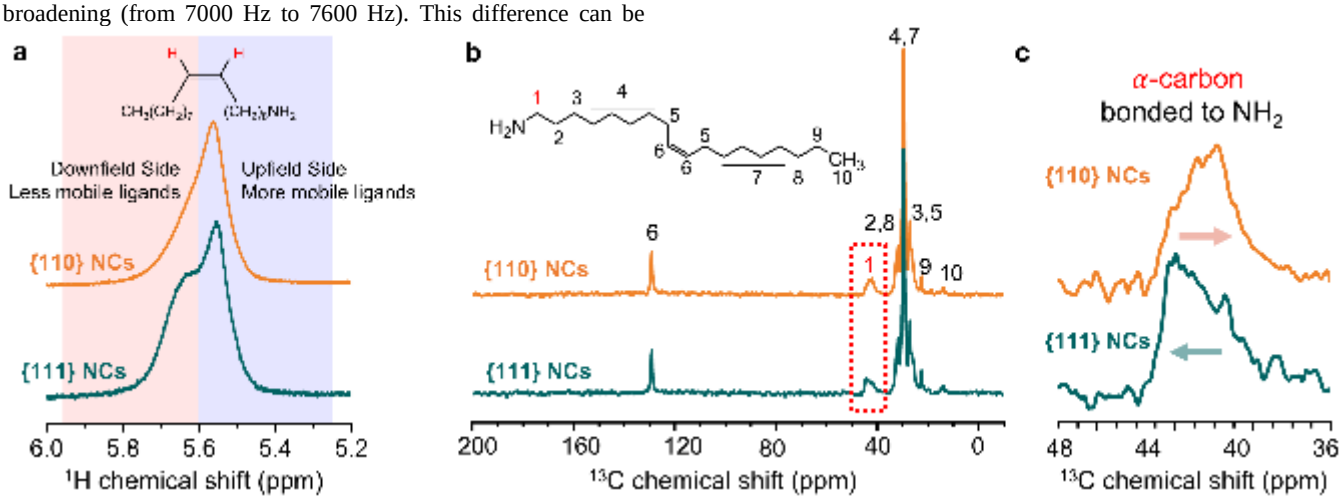

Figure 2 Characterization of organic ligands on the surface of faceted InP NCs (a) Solution ^{1}H NMR spectra for {110} NCs and {111} NCs in the region of the vinyl protons of the oleylamine ligand. (b) ^{1}H→^{13}C CP-MAS NMR for {110} NCs and {111} NCs. (c) The enlarged spectra from the red box in (b) showing the α-carbon adjacent to NH_2 group of oleylamine ligands.

with fewer edges/vertices. Consequently, this greater distribution of chemical shifts in {110} NCs compared to {111} NCs, despite both having an oleylamine chloride ligand system, is clearly observed. Moreover, when comparing the NMR data of our anisotropic NCs described herein with those of spherical InP NCs, the ^{31}P NMR chemical shift is little changed. However, the width of the corresponding resonances of the isotropic NCs significantly increases: 8800 Hz for InP NCs prepared from tris(diethylamino)phosphine and indium chloride in OLA[6] and 11300 Hz for InP NCs prepared from tris(trimethylsilyl)phosphine and indium acetate.[34] Only synthesis under mild conditions at 150°C using tris(trimethylsilyl)phosphine and indium amidinate[35] gives a FWHM close to those of our NCs, but without achieving such chemical shift homogeneity.

Characterization of the surface-ligand composition of {111} and {110} InP NCs

Solid-state NMR is sensitive and reliable in probing abundant information on chemical structure,[36, 37] ligand geometry,[38] spatial distance[39], and bonding environment,[38-40] including the acid strength and the effect of the Lewis acid and Brønsted acids.[41-43] Solution NMR also provides additional insights into molecular dynamics.[44] Therefore, we employed both solid-state and solution NMR to explore the surface-ligand composition. The difference in the chemical environment of oleylamine ligands bound on the two samples is observed by the solution ^{1}H NMR. Figure 2a shows an enlarged view of the olefin region of oleylamine, with distinctive differences in the olefin feature of {110} NCs and {111} NCs (See the entire ^{1}H solution NMR spectrum in Figure S18). Based on the previous study by Dümbgen *et al.*,[22] this is related to the dynamic differences of ligands when coordinated to edges, corners, and facets of the surface of NCs. The peak of the less mobile ligand region (red area) appears on the downfield side, while the more mobile ligand region (blue area) appears on the upfield side. The less mobile ligand region is more pronounced in {111} NCs than in {110} NCs (See deconvoluted spectra in Figure S5 and Table S1). This different contribution of less/more mobile ligands to the {111} and {110} NCs can be explained by the facet distributions and the portion of edges/corners at the surface of each NCs. As discussed in Figure 1, the tetrapodal geometry of {110} NCs yields relatively complex facet distributions (which is a combination of {110}/{-1-1-1} facets) and larger contributions of edges/corners when compared to the single-facet-terminated tetrahedral geometry of {111} NCs (Figure S1). As a result, the increased dynamics of bound ligands at the surface of {110} NCs result in the relatively higher portion of more mobile ligands in olefin signals.[22]

To further investigate the behavior of coordinated oleylamine ligands on the surface of NCs, ^{1}H→^{13}C cross-polarization (CP)-MAS NMR, where the transfer of polarization between H and C atoms is favored by restricted mobility, was performed (Figure 2b). The ^{1}H→^{13}C CP-MAS NMR spectra show the C=C oleylamine resonance at 129 ppm for both {110} NCs and {111} NCs. It indicates that the oleylamine ligands are coordinated to the surface of both {110} and {111} NCs,[6] which is also confirmed by the FT-IR spectra (Figure S6). This was further supported by the broadness of α–carbon resonance in both spectra. Notably, a different resonance feature of α-carbon neighboring to the NH_2 at the range from 40 ppm to 50 ppm, was observed in {110} NCs and {111} NCs. This demonstrates that the C-N chemical environments are strongly influenced by the {110} and {111} NCs surfaces, which is possibly the result of the two factors; 1) different electronic environments experienced by the oleylamine, which is in particular, the difference in Lewis acidity of {110} and {111} facets, and 2) the different orientation of ligand at NC surface, influenced by ligand packing at {110} and {111} facets. The {111} facets have unsaturat-

ed indium, which imparts it with stronger Lewis acidic properties relative to the {110} facets, where the indium are partially saturated by neighboring phosphorous atoms. This stronger Lewis acidity results in the deshielding of the α-carbon of the NH_2 group highlighted by the red box (Figure 2c).[45-46] Secondly, another reason may be related with the surface orientation of the oleylamine with respect to {110} and {111} surfaces. It has indeed been previously shown that molecular tilt may occur in order to favor ligand packing and increase their intermolecular Van der Waals (VdW) forces which is reflected as an energy shift in C-H vibrational stretches observed in FT-IR spectra.[37] Given the different surfaces, it is not surprising that different ligand organization takes place. However, FT-IR spectra of both {111} and {110} NCs show no difference in asymmetric (2920 cm^{-1}) and symmetric (2850 cm^{-1}) stretching vibration modes of carbon chain in oleylamine ligands (Figure S6 b); this suggests that despite their differences in facet distribution, shape geometry, and surface-to-volume ratio, both NCs exhibit minimal intermolecular VdW interactions. This is probably due to the relatively low oleylamine ligand density on both {111} and

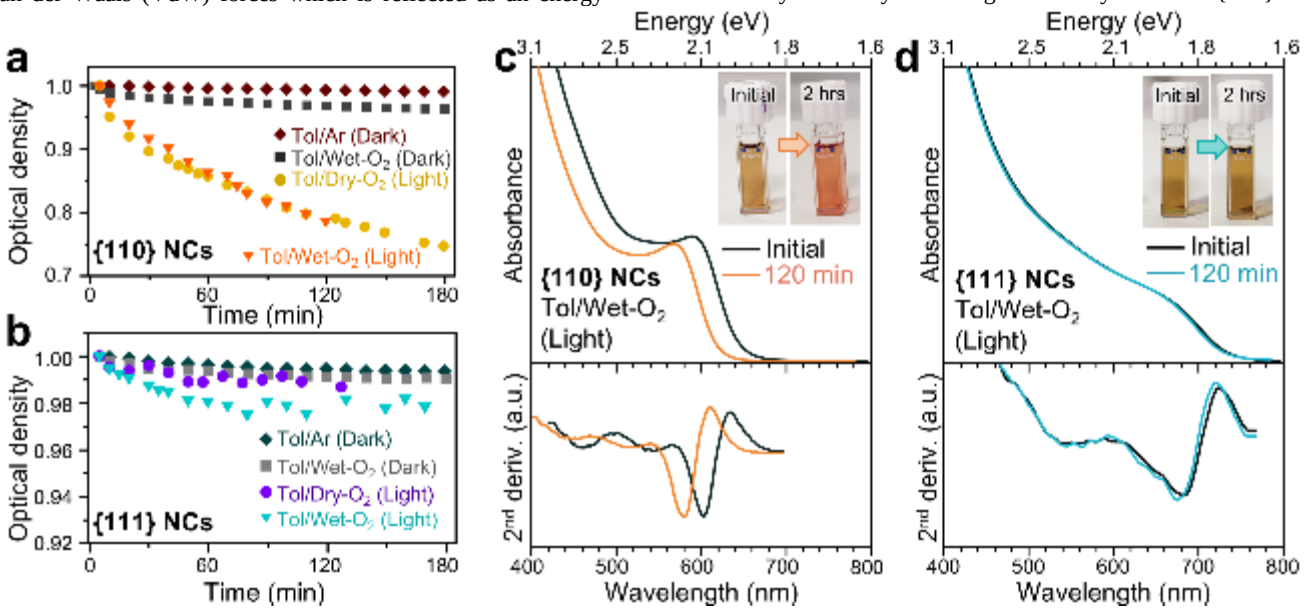

Figure 3. Optical properties for {110} NCs and {111} NCs. (a-b) Plot of the optical densities at 413 nm of excitation depicted from the absorbance spectra in Figure S8 and S9. (a) {110} NCs dispersions of toluene with saturated argon in the dark (brown diamond), wet-O_2 in the dark (black square), with dry-O_2 under the light (magenta circle), and with wet-O_2 under the light (orange triangle) (b) {111} NCs dispersions of toluene with saturated-argon in the dark (dark cyan diamond), wet-O_2 in the dark (grey square), with dry-O_2 under the light (violet circle), and with wet-O_2 under the light (cyan triangle). (c) The absorbance spectra of {110} NCs and (d) {111} NCs showing the peak shift of 1st excitonic transition after 120 min of light exposure depicted from the absorbance spectra in Figure S8 and S9. Inset are the pictures of NC dispersions in toluene with wet-O_2 under light. The second derivate curves are plotted at the bottom.

{110} NCs, because of the co-passivation with chloride ligands. Hence, a deshielded α-carbon resonance of oleylamine at {111} NCs (dark cyan) compared to {110} NCs (orange) is likely due to the strong Lewis acidity, with VdW interactions from ligand packing playing a negligible role. This also can lead to stronger ligand interactions.

Characterization of the InP inorganic core of {111} and {110} InP NCs after exposure to ambient.

The large portion of the surface in NCs makes their electronic and photophysical properties highly sensitive to the environmental species, such as electronic doping through oxygen adsorption or a decrease in photoluminescence due to structural degradation in ambient conditions.[48-50] Exploring the differences in surface reactivities of NCs with well-defined facets could provide insights into the chemistry needed to manipulate their photophysical properties across various environments.[25] In order to study their optical behavior according to the exposed facet of each NC, we exposed {111} and {110} NCs to air-saturated toluene (Tol/Wet-O_2). This solution was prepared by bubbling air into the toluene, resulting in a solution containing oxygen and moisture (water content of 115 ppm, see Table S2 and Figure S7). Figures 3a and b show the change of optical densities in absorbance spectra of {110} NCs and {111} NCs dispersed in air-saturated toluene. At the initial time, the absorbance spectra of the {111} and {110} NCs dispersions exhibit the same optical density at 413 nm, indicating that they have an equal number of In-P units.[14] As time goes by, comparing the absorbance spectra clearly shows the different behaviors of these NCs. The absorption spectra of {110} NCs exhibit a blue shift of 1st excitonic peak from 2.06 eV (601 nm) to 2.14 eV (579 nm) (0.12 nm decrease in NC size, estimated by Brus equation of InP nano wire[33]), accompanied by an overall degradation of optical density, corresponds to the observed color change from brown to orange (Figure 3a and c). In contrast, {111} NCs show only a slight change, with 0.02 eV shift (less than thermal energy at room temperature) of the 1st excitonic peak (sub-angstrom, 0.08 nm decrease in size estimated by Brus equation of tetrahedral InP NCs[23]), indicating that negligible etching occurred (Figure 3b and d). The photographs also show the color of {111} NCs dispersions at 0 hours and after 2 hours, indicating minimal change in color. The blue shift of the 1st excitonic peak typically implies a reduction in NC core size[49]; this also correlates with the decrease in optical density of NCs. The decrease in optical density at 413 nm excitation can be used to derive how many indium atoms are etched out from the core NC by using extinction coefficient per mole of NCs ($L \cdot mol^{-1} \cdot cm^{-1}$). Given that the single {111} and {110} NCs contain 1771 and 1400 indium atoms, respectively (Table S7), the number of etched indium atoms per the number of initial indium atoms and the number of indium atoms per surface area of each

NC are plotted (Figure S12). It is evident that the {110} NCs are significantly more sensitive to photooxidation compared to the {111} NCs, with approximately 20 % of indium atoms etched out, while less than 2.5 % of indium atoms are detached from the {111} NCs (Figure S12 (a)). Additionally, the reactivity per unit surface area of {110} NCs is $1.7x10^{-2}$ mol/min·nm^2, an order of magnitude higher than $1.9x10^{-3}$ mol/min·nm^2 of {111} NCs (Figure S12 (b)). Therefore, we concluded that {110} NCs were significantly influenced by air exposure, while {111} NCs were rather insensitive to the ambient environment.

Previous studies have shown that besides exposure to oxygen, water reacts with InP NCs and results in the oxidation of the surface.[51-53] To further investigate the process underlying the observed blue shift and to discriminate the relative effects of O_2 and H_2O, we used dried oxygen-saturated toluene (Tol/dry-O_2). Figures 3a and b display the plotted optical density change and Figure S10 a and b show the plotted 1st excitonic peak of {110} NCs and {111} NCs over time under the different exposure conditions. The corresponding absorbance spectra are shown in Figures S8

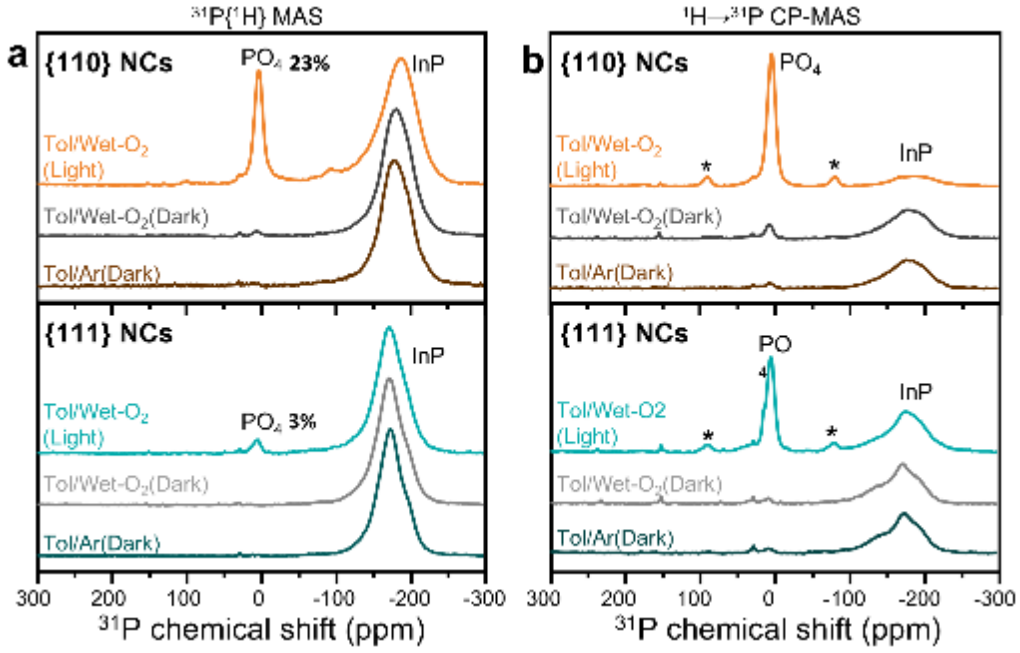

Figure 4 ^{31}P MAS NMR characterization for {110} NCs and {111} NCs under various environments. (a) ^{31}P{^{1}H} MAS NMR spectra and (b) ^{1}H→^{31}P CP-MAS NMR spectra of {110} NCs (top) and {111} NCs (bottom) under three different conditions: {110} NCs in Tol/Wet-O_2 under the light (orange), in Tol/Wet-O_2 in the dark (black), and Tol/Ar in the dark (brown); {111} NCs in Tol/Wet-O_2 under the light (cyan), in Tol/Wet-O_2 in the dark (light grey), and Tol/Ar (dark cyan). *: spinning side bands.

and S9. Comparing the air exposure and oxygen exposure under light, there is no significant difference when {110} NCs are exposed to wet or dry oxygen-containing toluene, suggesting that the impact of water is negligible in these conditions. Likewise, the presence of water does not impact to a marked degree the absorption maximum of the {111} NCs. In contrast, avoiding light irradiation has a dramatic effect. As can be seen in Figures 3 and S10, when NCs are placed in the dark, there is no change in the absorption spectra of the air-saturated solutions of {110} NCs and {111} NCs (Tol/wet-O_2). It clearly shows that the optical change was triggered by the presence of light. Thus, we could assume that the size decrease of NCs under the light in air-saturated toluene is largely related to the oxidation of the surface when the NC absorbs the light as the following reactions:[11, 51]

$$InP + (h\nu) \rightarrow e^- + h^+ \quad (1)$$

$$InP + e^-/h^+ + O_2 \rightarrow (InP + h^+) + O_2^{\bullet-} \quad (2)$$

$$(InP + 2h^+) + 2O_2^{\bullet-} \rightarrow InP + InPO_4 \quad (3)$$

Here, still, the curiosity remains about whether the oxidation really occurred at the surface of NCs when the 1st excitonic peak blue-shifts in the absorption spectra. The ^{31}P MAS NMR can provide the first hint (Figure 4a). After exposure to ambient in dark conditions (Tol/Wet-O_2 (dark)), no oxidized phosphorus was observed in the ^{31}P MAS NMR spectrum for {111} NCs (light grey) while a new peak at 5.6 ppm slightly appears for {110} NCs (black). By examining the ^{1}H→^{31}P CP-MAS NMR spectrum, this new resonance at 5.6 ppm is enhanced and can be confirmed as surface PO_4 moiety (Figure 4b).[4] CP is a key NMR technique for investigating the phosphorus species using polarization transfer from H to P atoms by dipolar coupling, which is associated with spatial proximity. Considering that this signal is hardly detected in the ^{31}P MAS NMR spectrum of {110} NCs, we could say that, under the dark conditions, only a very low amount (close to the detection limit of ~2%) of oxidized phosphorous exists at the surface of {110} and {111} InP NCs even with the presence of oxygen and moistures. On the other hand, shining light on the samples in ambient conditions (Tol/wet-O_2 (light)) results in changes to different extents. The {110} NCs show a significantly higher content of PO_4 (23 %, orange), while {111} NCs exhibit a low content of 3 % (cyan). This trend also aligns with the percentage of etched indium atoms in {110} and {111} NCs, as shown in Figure S12 a. In both NCs, the increase of the relative area of the PO_4 peak *vs.* the In-P one in the ^{1}H→ ^{31}P CP-MAS NMR spectra (Figure 4b) clearly shows that oxidation has occurred at the surface of the NCs.

The different air sensitivity of {110} and {111} NCs is also evident in the XPS analysis. We exposed the InP NCs thin films to air and observed the oxidation trend over time using lab-XPS (Figure S15). Remarkably, phosphate was not observed in the P 2p core spectrum of {111} InP NCs, suggesting that {111} facets have high air resistance even when prepared as a film type. Thus, we further analyzed oxidant species present on the indium surface using a synchrotron XPS, which is surface-

sensitive due to a short inelastic mean free path and has improved the resolution of the final spectra. We focused on In 3d and O 1s to compare the chemical surface states of {110} NCs and {111} NCs (See supporting discussion 3 for the detailed XPS measurements). According to the reference material, we were able to assign the peak component at 532 eV as hydroxide in O 1s core levels of {110} NCs, which also matches with the previous reports[52] (Figure S16 a). These results are also consistent with the In 3d XPS results showing that {110} NCs have a broader spectrum with increased contribution of higher binding energy region; this can be interpreted as increased In-O bonding moieties located in higher binding energy than In-P moieties (Figure S16 b).

In summary, these characterizations show that the blue-shift observed for the {110} NCs is the consequence of their oxidation with the conversion of surface InP into phosphates and hydroxide. Importantly, this phenomenon is triggered by light exposure, and the oxidation remains negligible in dark conditions. In contrast, and despite the same ligand species (which are oleylamine

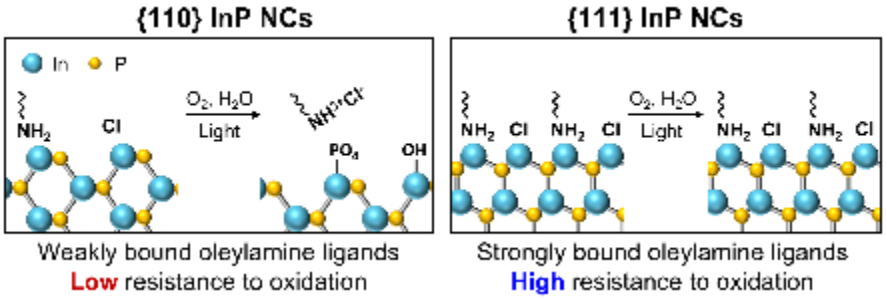

Figure 5 Schematic illustration of facet-dependent surface reactivities towards external molecules attributed from the Lewis acidity of different facets. As a result, this affects the binding strength of bound oleylamine and their different capping ligand densities.

and chloride), the behavior of {111} NCs is very different and displays high resistance to oxidation.

Discussions on the origin of facet-dependent reactivities of {111} and {110} InP NCs

The photo-assisted surface reactivity of NCs can be explained by two factors: 1) the band edge potentials matched with the redox potentials of a target reaction and 2) the active surface area where target reactant adsorption/desorption occurs. The conduction band minimum (CBM) is determined to be 3.28 eV for {111} NCs and 3.32 eV for {110} NC, considering the band gap energy of each NC and the valence band maximum measured by ambient photoemission spectroscopy (APS) (Figure S11). The first step in the photooxidation of InP NCs, equation (2), involves the transfer of an excited electron from the CBM of NCs to a dioxygen molecule. Therefore, we compared the oxygen reduction potential (O_2/O_2^-) with the CBM of each NCs (Table S3). The oxygen reduction potential of -0.18 V (vs. NHE)[54] corresponds to 4.26 eV (vs. vacuum), indicating a large potential barrier of approximately 1 eV exists between the CBMs of both {111} and {110} NCs. Given this large barrier and the room temperature thermal energy of 25 meV, the 40 meV difference in CBMs between two NCs is not substantial. Consequently, we concluded that the difference of conduction band edge potentials of {111} and {110} NCs is not a critical factor in explaining their differences in photooxidation behavior.

Secondly, the active surface area relative to the volume of the NC is determined by the surface-to-volume ratio (S/V) of the NCs. The surface-to-volume ratio is 3.10 for {110} NCs, which is larger than 1.78 of {111} NCs. To explore whether the higher reactivity of {110} NCs comes from the large surface-to-volume ratio, further experiments were conducted. Due to the narrow size range of tetrahedral {111} NCs that exhibit minimal truncation, we instead compared tetrapodal {110} NCs with both long and short arms, ensuring a similar surface-to-volume ratio but with different (110) surface areas (Figure S13 a). We hypothesize that, given the comparable surface-to-volume ratios and similar shape geometries, this comparison would reveal the (110) facet-dependence on reactivity toward photooxidation. The optical density and the peak shift of 1st excitonic transition of the two NCs were monitored under the light exposure in air-saturated toluene (Figure S13). The 1st excitonic peak shift and optical density decrease are larger for long {110} NCs compared to short {110} NCs. Since the amounts of NCs in the cuvette cell differs, the optical density was further converted to the percentage of decreased NC concentration and plotted (Figure S14). The concentration of each NC was estimated using the extinction coefficient per mole of NCs ($L \cdot mol^{-1} \cdot cm^{-1}$) which was obtained by ICP-OES measurement as described in the supporting discussion 4C. The percentage change in concentration of NCs also increases more rapidly for long {110} NCs than for short {110} NCs, which is consistent with a larger blue shift of 1st excitonic transition, indicating that InP core is etched out faster in long {110} NCs. Although they have similar surface-to-volume ratios (slightly smaller S/V for long {110} NCs), long {110} NCs possess 1.9 times larger surface area of (110) facet compared to short {110} NCs. This suggests that the reactivity difference arises from facet-dependent oxidation behavior rather than the surface-to-volume ratio.

In order to unravel the origin of the facet-dependent reactivities and, in particular, why the {111} NCs are resistant to oxidation, further studies on the behavior of surface ligands have been carried out. Since both {111} and {110} NCs are passivated with oleylamine ligands, which are long-chain organic molecules blocking the access of external oxidant species, their different reactivities to surface oxidation can be explained in two ways: 1) the density of surface ligand to block the access of oxidant molecules may be different, and 2) surface ligands could be detached from the surface due to the different binding strength to each NC surface.

Before exploring the density and the change of the bound oleylamine ligands, one critical fact should be confirmed. It has previously been reported that when NC surfaces are oxidized, ligand oxidation can also occur; thiol ligands being converted to disulfide ligands has been reported in the previous literature of CdSe NCs.[55] Oleylamine has a double bond which is electron-rich, and thus it is potentially prone to be oxidized in the presence of electron acceptor.[56, 57] Since the oleylamine ligands are quantified by using their olefin protons as a probe in ^{1}H NMR, we need to confirm first that the double bonds are not reacting to the oxidant species so that we are properly monitoring them in the system. Therefore, we compared the observed proton

ratios between olefin and -CH_3 protons of oleylamine in solution ^{1}H NMR under three different conditions (Tol/Ar;dark, Tol/Wet-O_2;dark, and Tol/Wet-O_2;light) (Table S4). The results showed that the proton ratios remained the same across all conditions, indicating that no ligand oxidation occurred, and thus, the number of oleylamine remains identical in the system.

Therefore, we first calculated the ligand density (nm^{-2}) of surface oleylamine on each {111} and {110} NCs (Table S5; see supporting discussion 4 for details), which can influence the surface oxidation of NCs by affecting the access of oxidant molecules. Along with the multiple washing steps, the ligand densities of two NCs are saturated to the specific value (Table S6). The resulting values show that fewer oleylamine ligands (0.79 nm^{-2}) are present on the surface of {110} NCs when compared to 1.17 nm^{-2} of oleylamine coverage for {111} NCs; this is consistent with the previous surface passivation models from DFT calculations.[32,33] The most energetically favorable binding motifs for the (111) facet is chloride/amine co-passivation,[33] with the estimated amine coverage of 1.65 nm^{-2} when fully passivated (Figure S19). For the (110) facet, $InCl_3$ is the most stable motif, with a minor energy difference for $InCl_2$ with amine derivative, and InCl for the (-1-1-1) facet terminated by P atoms.[33] This results in a lower oleylamine density on {110} NCs compared to the {111} NCs. Additionally, even when the surface adopts the most stable binding motifs that fully passivate the surface, the non-polar (110) surface still exhibits 2.03/nm^2 of uncoordinated P atoms (Figure R19 (b)), whereas the polar (111) and (-1-1-1) surfaces are fully passivated in their most stable binding forms (Figure R19 (a)). This undercoordinated surface atom also may contribute to the large surface oxidation of {110} NCs. Secondly, the ligands at the surface of each faceted InP NC are also monitored to see whether they are detached after exposure to air (Tol/wet-O_2) under light for both {110} NCs and {111} NCs. From the solution ^{1}H NMR spectra, we observed that oleylammonium species are formed after {110} NCs are exposed to air under light (Figure S18). In contrast, {111} NCs show negligible formation of oleylammonium. Oleylammonium can be formed when the oleylamine receives a proton from H_2O in the air, and this may be resulted from the surface oleylamine detachment since the whole olefin protons are kept identical in the system. Based on the previous discussion, this may be related to the differences in ligand bonding strength between the {110} and {111} facets. The {111} facet has stronger Lewis acidity than the {110} facet, allowing ligands to bind more strongly. Consistent with the results in previous discussions showing that the {110} NCs have relatively more mobile oleylamine ligands due to the large portion of edges and corners at the NCs, their ligands are more prone to desorption from the surface. The detached ligands further react with H_2O in the ambient atmosphere, leading to the formation of oleylammonium. The difference in binding strength is also supported by the DFT calculations from previous literature showing that (110) facet has lower ligand binding strength to oleylamine/chloride ligands when compared to (111) facet.[33]

To sum up, the {111} NCs have stronger Lewis acidity and relatively small surface heterogeneity (indium-terminated single {111} facets with lower contribution of edges/corners) with smaller surface-to-volume ratio and also exhibit higher ligand density on the NC surface when compared to {110} NCs. The strongly bound ligands preventing desorption from the NC surface are confirmed by the absence of oleylammonium formation (Figure 5). On the other hands, the {110} NCs, which have predominant (110) facets with lower ligand density, larger contribution of edge/vertex on surface, and larger surface-to-volume ratios due to the tetrapodal shape geometry, also possesses lower binding strength to surface ligands. Thereby, {111} NCs result in greater oxidation resistance.

CONCLUSION

In this study, we explored the facet-dependent reactivities of InP NCs towards the ambient species through a combination of spectroscopic analysis. The well-defined InP NCs having {111} and {110}/{-1-1-1} facets are synthesized under the same chloride/oleylamine ligand conditions. More complex facet distribution, as well as the lower Lewis-acidic surface in {110} NCs, when compared to the {111} NCs were confirmed by broad ^{31}P and ^{115}In resonances and shielded α-carbon ^{13}C resonances in MAS NMR studies. Notably, the resulting {111} NCs exhibit lower reactivity towards external ambient molecules under light irradiation, showing a minimal blue shift in 1st excitonic peak and optical density at 413 nm excitation in absorption spectra.[14] This higher resistance could be explained by stronger ligand binding, higher ligand density, and a more distinctive presence of less mobile oleylamine ligands on the NC surface; this could be attributed to the stronger Lewis acidity of {111} surface as well as the lower edge/corner contribution and the single-facet termination of {111} NC. Furthermore, by finely tuning the arm width and length of well-defined {110} NCs, while ensuring a consistent surface-to-volume ratio but varying the (110) surface area, we were able to explore the (110) facet-dependent photooxidation reactivity. Solid-state/solution NMR and XPS analyses also support these findings by showing distinct differences in the surface phosphate and hydroxyl amount and probing the presence of displaced oleylammonium species from the {110} NCs and {111} NCs.

We believe that our findings are crucial for understanding and improving the facet-originated reactivity and stability of InP NCs in various applications, and in particular, suggesting {111} facets as a strategy to enhance the atmospheric stability of InP NCs even in the ambient conditions. As the development of next-generation colloidal NCs with superior photophysical properties and high uniformity depends heavily on mastering NC surface characteristics, this approach offers strategic insight into surface manipulation to optimize their photophysical behavior. This becomes particularly valuable when compared to less-defined NCs, where surface properties remain ambiguous for targeted applications. Continued efforts in this area will provide valuable pathways for enhancing NC performance, even when precise facet control is not fully achievable.

EXPERIMENTAL SECTION

Chemicals

All chemicals were stored and treated in a N_2-filled glove box as received unless stated explicitly. Indium chloride ($InCl_3$, 98%), tris(dimethylamino)phosphine (DMA_3P), 97%), oleylamine (70%) were purchased from Sigma-Aldrich. Lithium bis(trimethylsilyl)amide (or lithium hexamethyldisilazide, LiHMDS, 97%) was purchased from thermo scientific. Degassed oleylamine was prepared by degassing under vacuum (~0.2 torr) around 140 °C for 60 min.

Synthesis of {110} InP NCs

The synthesis followed the procedure reported by Kim *et al.*[33] In a 100 mL three-necked round bottom flask, 1.129 g (5 mmol) indium (III) chloride and distilled oleylamine (25 mL, 76 mmol) were stirred and degassed at 110 °C under vacuum (~0.2 torr) for one hour. For the preparation of the P-precursor, 0.937 mL

(5 mmol) DMA_3P was loaded into a syringe with mixed oleylamine. The mixed oleylamine was prepared by stirring 0.084 g (0.5 mmol) LiHMDS and 2.5 mL distilled oleylamine at 60 °C for 20 minutes in a N_2-filled glove box. The P-precursor was then injected into the indium-oleylamine reaction mixture at 170 °C and held for one hour. The temperature was then increased from 170 °C to 280 °C for 10 minutes and cooled to room temperature. The as-synthesized InP NCs are transferred to a N_2-filled glove box and precipitated using anhydrous butanol, anhydrous acetonitrile, and anhydrous hexane or anhydrous toluene. For characterization, this purification step was repeated more than twice. The as-synthesized NC dispersions are stored in the dark inside an N_2-filled glove box until use.

Synthesis of {111} InP NCs

The experimental processes for synthesizing the {111} InP NCs were the same as those for the {110} InP NCs, except for the preparation of P-precursor and the reaction conditions. To synthesize of {111} InP NCs, the P-precursor was prepared by mixing 0.937 mL (5 mmol) DMA_3P with 2.5 mL of distilled oleylamine. Subsequently, the P-precursor was injected into the indium-oleylamine reaction mixture at 250 °C and kept for 30 minutes. The as-synthesized NC dispersions are transferred in an N_2-filled glove box. Purification was performed as same with {110} NCs.

General Characterization

The UV-vis spectra were recorded using an Agilent Cary 5000 UV-Vis-NIR spectrophotometer. To obtain the spectra under inert-atmosphere, cuvette with the screw cap was used. The laboratory atmosphere has 28~38 % humidity at room temperature (22.4~23.4 °C). The amount of H_2O was measured by Karl Fischer Moisture Analyzer using the Metrohm 831 KF Coulometer. For transmission electron microscopy (TEM) images, spherical aberration-corrected TEM (JEOL, JEM-ARM 200 F) was used with an acceleration voltage of 60 kV for {111} NCs and 300 kV for {110} NCs, respectively. For TEM sample preparation, InP NCs solution dispersed in toluene was drop-cast onto an ultrathin carbon purchased from Ted Pella. FT IR spectra were obtained using an IRTracer-100 (Shimadzu) with 8 cm^{-1} resolution and diamond attenuated total reflection (ATR) accessory. The FT IR sample was deposited on the Si/Cr/Au substrate.

X-ray Photoelectron Spectroscopy

XPS spectra were obtained using Prevac ESCA 2000 instruments. The excitation source was a monochromized Al Ka X-ray source at 1486.7 eV operated at 16.6 mA and 12.0 kV. The pressure in the analytical chamber during the spectral acquisition was $<8*10^{-9}$ mbar. For the XPS sample preparation, the InP NCs solution was loaded into a 1 mL syringe and filtered using a 0.25 μm pore size PVDF syringe filter. It was then spin-coated onto the Si/Cr/Au substrate. All sample preparation was performed in a N_2-filled glove box and the sample thickness of 10 to 20 nm was used to avoid charging effects during XPS measurements. The InP NCs films were transferred using sealed containers to the instrument. The air-exposed samples were put outside which atmosphere have 25 % humidity at room temperature (around 23.6 °C). The binding energy calibration was performed using the C 1s binding energy (284.8 eV). The pass energy was 50 eV for narrow scan and 100 eV for survey scan. The high-resolution XPS spectra were obtained using a synchrotron radiation X-ray source at the 10A2 HR-PES II beamline of the Pohang Accelerator Laboratory (PAL, Republic of Korea). The excitation energy was calibrated to 84 eV gold binding energy using Au foil. The pass energy was 20 eV for narrow scan.

Solid-State Nuclear Magnetic Resonance Spectroscopy

The dried, powder type InP NCs sample was taken and transferred to a 3.2 mm zirconia rotor under argon-filled glove box. The rotor was tightly sealed using the cap and no sign of air contamination was detected. NMR spectra were recorded on a Bruker Avance III HD 400 or Avance NEO 600 spectrometers. The rotors were spun between 8 to 18 kHz at room temperature. For ^1H MAS were performed with the DEPTH pulse sequence and a recycle delay of 5 s. $^{31}P\{^1H\}$ MAS were acquired with a Hahn-echo synchronized with the spinning rate and a recycle delay of 60 s. ^{13}C CP-MAS and ^{31}P CP-MAS spectra were recorded with a recycle delay of 2 s and contact times of 2 ms, 0.5 ms and 5 ms, respectively. Static ^{115}In Hahn-echo spectra were obtained with a recycle delay of 0.1 s. All chemical shifts for ^1H and ^{13}C are relative to TMS. ^{31}P and ^{115}In chemical shifts were referenced with respect to external solutions of 85% H_3PO_4 and 0.1 M $In(NO_3)_3$, respectively.

Liquid-state Nuclear Magnetic Resonance Spectroscopy

The InP NCs were dissolved in 500 uL of toluene-d8 under N_2 atmosphere. The optical density of InP NC solutions used for NMR measurement are 1.6 in absorbance spectra when diluted (a dilution factor of 151). ^1H NMR measurement were recorded at T= 298 K using a Bruker at the Chiral Material Core Facility Center of Sungkyunkwan University. NMR is operated at ^1H frequency of 500.13 MHz with 20 s delay of D_1 time. The detailed quantitative analysis was shown in Supporting discussion 4.

ASSOCIATED CONTENT

Supporting Information

This material is available free of charge via the Internet at http://pubs.acs.org."

Additional characterization (FT IR, XRD, XPS), optical properties, oleylamine density of faceted InP NCs.

AUTHOR INFORMATION

Corresponding Author

*Sohee Jeong - Department of Energy Science (DOES), Center for Artificial Atoms, and Sungkyunkwan Institute of Energy Science and Technology (SIEST), Sungkyunkwan University (SKKU), Suwon, Gyeonggi-do 16419, Republic of Korea; orcid.org/0000-0002-9863-1374; Email: s.jeong@skku.edu

*Fabien Delpech- Laboratoire de Physique et Chimie des Nano-Objets (LPCNO), Université de Toulouse, CNRS, INSA, UPS, 31077 Toulouse Cedex 4, France; orcid.org/ 0000-0003-1517-1331; E-mail: fdelpech@insa-toulouse.fr.

Authors

Eunhye Cho- Department of Energy Science (DOES) and Center for Artificial Atoms, Sungkyunkwan University (SKKU), Suwon, Gyeonggi-do 16419, Republic of Korea; orcid.org/0000-0003-0229-9520

Meeree Kim- Department of Energy Science (DOES) and Center for Artificial Atoms, Sungkyunkwan University (SKKU), Suwon, Gyeonggi-do 16419, Republic of Korea; orcid.org/0000-0001-9183-0517

Liyan Ouyang- Laboratoire de Physique et Chimie des Nano-Objets (LPCNO), Université de Toulouse, CNRS, INSA, UPS, 31077 Toulouse Cedex 4, France; orcid.org/0000-0002-5858-5297

Hyoin Kim- Department of Energy Science (DOES) and Center for Artificial Atoms, Sungkyunkwan University (SKKU), Suwon, Gyeonggi-do 16419, Republic of Korea; orcid.org/0000-0002-3967-7153

Guillaume Bonifas- Laboratoire de Physique et Chimie des Nano-Objets (LPCNO), Université de Toulouse, CNRS, INSA, UPS, 31077 Toulouse Cedex 4, France; orcid.org/0009-0005-3757-8329

Yannick Coppel- Laboratoire de Chimie de Coordination, CNRS, UPR 8241, Université de Toulouse, 31077 Toulouse, France; orcid.org/0000-0003-0970-4082

Céline Nayral- Laboratoire de Physique et Chimie des Nano-Objets (LPCNO), Université de Toulouse, CNRS, INSA, UPS, 31077 Toulouse Cedex 4, France; orcid.org/

Author Contributions

The manuscript was written through contributions of all authors. All authors have given approval to the final version of the manuscript. #These authors (Eunhye Cho, Meeree Kim) contributed equally to this work.

Notes

The authors declare no competing financial interest.

ACKNOWLEDGMENT

The authors gratefully thank Angélique Gillet, Adeline Pham, and Simon Cayez for technical support and Hangil Lee for the assistance in XPS measurement. This research was supported by the Creative Materials Discovery Program through the National Research Foundation (NRF) of Korea (NRF-2019M3D1A1078299), an NRF grant funded by the MSIT (2021K1A3A1A21039697, NRF-2020M3H4A3081813, NRF2022R1A2C2091486, and NRF-2022M3H4A1A03076626) and Korea Basic Science Institute (National research Facilities and Equipment Center) grant funded by the Ministry of Education (2022R1A6C101A751)

This research was also funded by the PHC STAR n°47416VF and ANR-21-CE09-0030-05, the Université Paul Sabatier, the Centre National de Recherche Scientifique (CNRS), the Institut National des Sciences Appliquées (INSA) of Toulouse, the French Ministry of Europe and Foreign Affairs (MEAE) and the French Ministry of Higher Education and Research (MESR).

M.K. is supported by Basic Science Research Program through the National Research Foundation of Korea (NRF) funded by the Ministry of Education (2022R1A6A3A0108754111 and RS-2024-00461815).

REFERENCES

(1) Guzelian, A. A.; Banin, U.; Kadavanich, A. V.; Peng, X.; Alivisatos, A. P. Colloidal chemical synthesis and characterization of InAs nanocrystal quantum dots. *Appl. Phys. Lett.* **1996**, *69*, 1432-1434.

(2) Micic, O. I.; Curtis, C. J.; Jones, K. M.; Sprague, J. R.; Nozik, A. J. Synthesis and Characterization of InP Quantum Dots. *J. Phys. Chem.* **1994**, *98*, 4966-4969.

(3) Murray, C. B.; Norris, D. J.; Bawendi, M. G. Synthesis and characterization of nearly monodisperse CdE (E = sulfur, selenium, tellurium) semiconductor nanocrystallites. *J. Am. Chem. Soc.* **1993**, *115*, 8706-8715.

(4) Stam, M.; Almeida, G.; Ubbink, R. F.; van der Poll, L. M.; Vogel, Y. B.; Chen, H.; Giordano, L.; Schiettecatte, P.; Hens, Z.; Houtepen, A. J. Near-Unity Photoluminescence Quantum Yield of Core-Only InP Quantum Dots via a Simple Postsynthetic InF_3 Treatment. *ACS Nano* **2024**, *18*, 14685-14695.

(5) Kirkwood, N.; Monchen, J. O. V.; Crisp, R. W.; Grimaldi, G.; Bergstein, H. A. C.; du Fossé, I.; van der Stam, W.; Infante, I.; Houtepen, A. J. Finding and Fixing Traps in II–VI and III–V Colloidal Quantum Dots: The Importance of Z-Type Ligand Passivation. *J. Am. Chem. Soc.* **2018**, *140*, 15712-15723.

(6) Tessier, M. D.; Baquero, E. A.; Dupont, D.; Grigel, V.; Bladt, E.; Bals, S.; Coppel, Y.; Hens, Z.; Nayral, C.; Delpech, F. Interfacial Oxidation and Photoluminescence of InP-Based Core/Shell Quantum Dots. *Chem. Mater.* **2018**, *30*, 6877-6883.

(7) Kroupa, D. M.; Vörös, M.; Brawand, N. P.; McNichols, B. W.; Miller, E. M.; Gu, J.; Nozik, A. J.; Sellinger, A.; Galli, G.; Beard, M. C. Tuning colloidal quantum dot band edge positions through solution-phase surface chemistry modification. *Nat. Commun.* **2017**, *8*, 15257.

(8) Choi, M.; Kim, M.; Lee, Y.; Kim, T.; Kim, J. H.; Shin, D.; Kim, J. W.; Kim, Y.-H.; Jeong, S. Tailored Band Edge Positions by Fractional Ligand Replacement of Nonconductive Colloidal Quantum Dot Films. *J. Phys. Chem. C* **2023**, *127*, 4825-4832.

(9) Brown, P. R.; Kim, D.; Lunt, R. R.; Zhao, N.; Bawendi, M. G.; Grossman, J. C.; Bulović, V. Energy Level Modification in Lead Sulfide Quantum Dot Thin Films through Ligand Exchange. *ACS Nano* **2014**, *8*, 5863-5872.

(10) Ko, J.; Jeong, B. G.; Chang, J. H.; Joung, J. F.; Yoon, S.-Y.; Lee, D. C.; Park, S.; Huh, J.; Yang, H.; Bae, W. K.; Jang, S. G.; Bang, J. Chemically resistant and thermally stable quantum dots prepared by shell encapsulation with cross-linkable block copolymer ligands. *NPG Asia Mater.* **2020**, *12*, 19.

(11) Zhang, J.; Li, J.; Ye, Z.; Cui, J.; Peng, X. Hot-Electron-Induced Photochemical Properties of CdSe/ZnSe Core/Shell Quantum Dots under an Ambient Environment. *J. Am. Chem. Soc.* **2023**, *145*, 13938-13949.

(12) Choi, H.; Ko, J.-H.; Kim, Y.-H.; Jeong, S. Steric-Hindrance-Driven Shape Transition in PbS Quantum Dots: Understanding Size-Dependent Stability. *J. Am. Chem. Soc.* **2013**, *135*, 5278-5281.

(13) Gary, D. C.; Terban, M. W.; Billinge, S. J. L.; Cossairt, B. M. Two-Step Nucleation and Growth of InP Quantum Dots via Magic-Sized Cluster Intermediates. *Chem. Mater.* **2015**, *27*, 1432-1441.

(14) Tessier, M. D.; Dupont, D.; De Nolf, K.; De Roo, J.; Hens, Z. Economic and Size-Tunable Synthesis of InP/ZnE (E = S, Se) Colloidal Quantum Dots. *Chem. Mater.* **2015**, *27*, 4893-4898.

(15) Clarke, M. T.; Viscomi, F. N.; Chamberlain, T. W.; Hondow, N.; Adawi, A. M.; Sturge, J.; Erwin, S. C.; Bouillard, J.-S. G.; Tamang,

S.; Stasiuk, G. J. Synthesis of super bright indium phosphide colloidal quantum dots through thermal diffusion. *Commun. Chem.* **2019**, *2*, 36.

(16) Kim, T.; Park, S.; Jeong, S. Diffusion dynamics controlled colloidal synthesis of highly monodisperse InAs nanocrystals. *Nat. Commun.* **2021**, *12*, 3013.

(17) Yoon, J. I.; Kim, H.; Kim, M.; Cho, H.; Kwon, Y. A.; Choi, M.; Park, S.; Kim, T.; Lee, S.; Jo, H.; Kim, B.; Cho, J. H.; Park, J.-S.; Jeong, S.; Kang, M. S. P- and N-type InAs nanocrystals with innately controlled semiconductor polarity. *Sci. Adv.* **2023**, *9*, eadj8276.

(18) Drijvers, E.; De Roo, J.; Martins, J. C.; Infante, I.; Hens, Z. Ligand Displacement Exposes Binding Site Heterogeneity on CdSe Nanocrystal Surfaces. *Chem. Mater.* **2018**, *30*, 1178-1186.

(19) Zhang, J.; Zhang, H.; Cao, W.; Pang, Z.; Li, J.; Shu, Y.; Zhu, C.; Kong, X.; Wang, L.; Peng, X. Identification of Facet-Dependent Coordination Structures of Carboxylate Ligands on CdSe Nanocrystals. *J. Am. Chem. Soc.* **2019**, *141*, 15675-15683.

(20) Kessler, M. L.; Dempsey, J. L. Mapping the Topology of PbS Nanocrystals through Displacement Isotherms of Surface-Bound Metal Oleate Complexes. *Chem. Mater.* **2020**, *32*, 2561-2571.

(21) Kim, M.; Choi, M.; Choi, S.; Jeong, S. Semiconductor Nanocrystals: Unveiling the Chemistry behind Different Facets. *Acc. Chem. Res.* **2023**, *56*, 1756-1765.

(22) Dümbgen, K. C.; Infante, I.; Hens, Z. Localizing Oleylamine Ligands on Amine–Halide Copassivated Indium Phosphide Nanocrystals. *Chem. Mater.* **2023**, *35*, 4393-4403.

(23) Kim, M.; Lee, J.; Jung, J.; Shin, D.; Kim, J.; Cho, E.; Xing, Y.; Jeong, H.; Park, S.; Oh, S. H.; Kim, Y.-H.; Jeong, S. Surface-Originated Weak Confinement in Tetrahedral Indium Arsenide Quantum Dots. *J. Am. Chem. Soc.* **2024**, *146*, 10251-10256.

(24) Bae, W. K.; Joo, J.; Padilha, L. A.; Won, J.; Lee, D. C.; Lin, Q.; Koh, W.-k.; Luo, H.; Klimov, V. I.; Pietryga, J. M. Highly Effective Surface Passivation of PbSe Quantum Dots through Reaction with Molecular Chlorine. *J. Am. Chem. Soc.* **2012**, *134*, 20160-20168.

(25) Woo, J. Y.; Ko, J.-H.; Song, J. H.; Kim, K.; Choi, H.; Kim, Y.-H.; Lee, D. C.; Jeong, S. Ultrastable PbSe Nanocrystal Quantum Dots via in Situ Formation of Atomically Thin Halide Adlayers on PbSe(100). *J. Am. Chem. Soc.* **2014**, *136*, 8883-8886.

(26) Busby, E.; Anderson, N. C.; Owen, J. S.; Sfeir, M. Y. Effect of Surface Stoichiometry on Blinking and Hole Trapping Dynamics in CdSe Nanocrystals. *J. Phys. Chem. C* **2015**, *119*, 27797-27803.

(27) Tan, C.-S.; Chen, H.-S.; Chiu, C.-Y.; Wu, S.-C.; Chen, L.-J.; Huang, M. H. Facet-Dependent Electrical Conductivity Properties of PbS Nanocrystals. *Chem. Mater.* **2016**, *28*, 1574-1580.

(28) Xia, Y.; Chen, W.; Zhang, P.; Liu, S.; Wang, K.; Yang, X.; Tang, H.; Lian, L.; He, J.; Liu, X.; Liang, G.; Tan, M.; Gao, L.; Liu, H.; Song, H.; Zhang, D.; Gao, J.; Wang, K.; Lan, X.; Zhang, X.; Müller-Buschbaum, P.; Tang, J.; Zhang, J. Facet Control for Trap-State Suppression in Colloidal Quantum Dot Solids. *Adv. Funct. Mater.* **2020**, *30*, 2000594.

(29) Cao, Y.; Stavrinadis, A.; Lasanta, T.; So, D.; Konstantatos, G. The role of surface passivation for efficient and photostable PbS quantum dot solar cells. *Nat. Energy* **2016**, *1*, 16035.

(30) Kim, Y.; Che, F.; Jo, J. W.; Choi, J.; García de Arquer, F. P.; Voznyy, O.; Sun, B.; Kim, J.; Choi, M.-J.; Quintero-Bermudez, R.; Fan, F.; Tan, C. S.; Bladt, E.; Walters, G.; Proppe, A. H.; Zou, C.; Yuan, H.; Bals, S.; Hofkens, J.; Roeffaers, M. B. J.; Hoogland, S.; Sargent, E. H. A Facet-Specific Quantum Dot Passivation Strategy for Colloid Management and Efficient Infrared Photovoltaics. *Adv. Mater.* **2019**, *31*, 1805580.

(31) Shi, G.; Wang, H.; Zhang, Y.; Cheng, C.; Zhai, T.; Chen, B.; Liu, X.; Jono, R.; Mao, X.; Liu, Y.; Zhang, X.; Ling, X.; Zhang, Y.; Meng, X.; Chen, Y.; Duhm, S.; Zhang, L.; Li, T.; Wang, L.; Xiong, S.; Sagawa, T.; Kubo, T.; Segawa, H.; Shen, Q.; Liu, Z.; Ma, W. The effect of water on colloidal quantum dot solar cells. *Nat. Commun.* **2021**, *12*, 4381.

(32) Kim, K.; Yoo, D.; Choi, H.; Tamang, S.; Ko, J.-H.; Kim, S.; Kim, Y.-H.; Jeong, S. Halide–Amine Co-Passivated Indium Phosphide Colloidal Quantum Dots in Tetrahedral Shape. *Angew. Chem. Int. Ed.* **2016**, *55*, 3714-3718.

(33) Kim, Y.; Choi, H.; Lee, Y.; Koh, W.-k.; Cho, E.; Kim, T.; Kim, H.; Kim, Y.-H.; Jeong, H. Y.; Jeong, S. Tailored growth of single-crystalline InP tetrapods. *Nat. Commun.* **2021**, *12*, 4454.

(34) Cros-Gagneux, A.; Delpech, F.; Nayral, C.; Cornejo, A.; Coppel, Y.; Chaudret, B. Surface Chemistry of InP Quantum Dots: A **Comprehensive** Study. *J. Am. Chem. Soc.* 2010, *132*, 18147-18157.

(35) Tamang, S.; Lincheneau, C.; Hermans, Y.; Jeong, S.; Reiss, P. Chemistry of InP Nanocrystal Syntheses. *Chem. Mater.* **2016**, *28* (8), 2491-2506.

(36) Virieux, H.; Le Troedec, M.; Cros-Gagneux, A.; Ojo, W.-S.; Delpech, F.; Nayral, C.; Martinez, H.; Chaudret, B. InP/ZnS Nanocrystals: Coupling NMR and XPS for Fine Surface and Interface Description. *J. Am. Chem. Soc.* **2012**, *134*, 19701-19708.

(37) Lovingood, D. D.; Achey, R.; Paravastu, A. K.; Strouse, G. F. Size- and Site-Dependent Reconstruction in CdSe QDs Evidenced by ^{77}Se{^{1}H} CP-MAS NMR Spectroscopy. *J. Am. Chem. Soc.* **2010**, *132*, 3344-3354.

(38) Baquero, E. A.; Ojo, W.-S.; Coppel, Y.; Chaudret, B.; Urbaszek, B.; Nayral, C.; Delpech, F. Identifying short surface ligands on metal phosphide quantum dots. *Phys. Chem. Chem. Phys.* **2016**, *18*, 17330-17334,

(39) Hanrahan, M. P.; Stein, J. L.; Park, N.; Cossairt, B. M.; Rossini, A. J. Elucidating the Location of Cd^{2+} in Post-synthetically Treated InP Quantum Dots Using Dynamic Nuclear Polarization ^{31}P and ^{113}Cd Solid-State NMR Spectroscopy. *J. Phys. Chem. C* **2021**, *125*, 2956-2965.

(40) Piveteau, L.; Ong, T.-C.; Rossini, A. J.; Emsley, L.; Copéret, C.; Kovalenko, M. V. Structure of Colloidal Quantum Dots from Dynamic Nuclear Polarization Surface Enhanced NMR Spectroscopy. *J. Am. Chem. Soc.* **2015**, *137* (43), 13964-13971.

(41) Fu, Y.; Zhang, L.; Yue, B.; Chen, X.; He, H. Simultaneous Characterization of Solid Acidity and Basicity of Metal Oxide Catalysts via the Solid-State NMR Technique. *J. Phys. Chem. C* **2018**, *122*, 24094-24102.

(42) Zhang, W.; Lin, Z.; Li, H.; Wang, F.; Wen, Y.; Xu, M.; Wang, Y.; Ke, X.; Xia, X.; Chen, J.; Peng, L. Surface acidity of tin dioxide nanomaterials revealed with ^{31}P solid-state NMR spectroscopy and DFT calculations. *RSC Adv.* **2021**, *11*, 25004-25009

(43) Chen, Y.; Dorn, R. W.; Hanrahan, M. P.; Wei, L.; Blome-Fernández, R.; Medina-Gonzalez, A. M.; Adamson, M. A. S.; Flintgruber, A. H.; Vela, J.; Rossini, A. J. Revealing the Surface Structure of CdSe Nanocrystals by Dynamic Nuclear Polarization-Enhanced ^{77}Se and ^{113}Cd Solid-State NMR Spectroscopy. *J. Am. Chem. Soc.* **2021**, *143*, 8747-8760.

(44) De Roo, J.; Yazdani, N.; Drijvers, E.; Lauria, A.; Maes, J.; Owen, J. S.; Van Driessche, I.; Niederberger, M.; Wood, V.; Martins, J. C.; Infante, I.; Hens, Z. Probing Solvent–Ligand Interactions in Colloidal Nanocrystals by the NMR Line Broadening. *Chem. Mater.* **2018**, *30*, 5485-5492.

(45) Spataro, G.; Champouret, Y.; Florian, P.; Coppel, Y.; Kahn, M. L. Multinuclear solid-state NMR study: a powerful tool for understanding the structure of ZnO hybrid nanoparticles. *Phys. Chem. Chem. Phys.* **2018**, *20*, 12413-12421

(46) Hu, Y.; Guo, B.; Fu, Y.; Ren, Y.; Tang, G.; Chen, X.; Yue, B.; He, H. Facet-dependent acidic and catalytic properties of sulfated titania solid superacids. *Chem. Commun.* **2015**, *51*, 14219-14222

(47) Meulenberg, R. W.; Strouse, G. F. Chain Packing Analysis of the Passivating Layer on Nanocrystalline Quantum Dot Surfaces. *J. Phys. Chem. B* **2001**, *105*, 7438-7445.

(48) Zhang, Y.; Zherebetskyy, D.; Bronstein, N. D.; Barja, S.; Lichtenstein, L.; Alivisatos, A. P.; Wang, L.-W.; Salmeron, M. Molecular Oxygen Induced in-Gap States in PbS Quantum Dots. *ACS Nano* **2015**, *9*, 10445-10452.

(49) Baek, H.; Kang, S.; Heo, J.; Choi, S.; Kim, R.; Kim, K.; Ahn, N.; Yoon, Y.-G.; Lee, T.; Chang, J. B.; Lee, K. S.; Park, Y.-G.; Park, J. Insights into structural defect formation in individual InP/ZnSe/ZnS quantum dots under UV oxidation. *Nat. Commun.* **2024**, *15*, 1671.

(50) Hines, D. A.; Becker, M. A.; Kamat, P. V. Photoinduced Surface Oxidation and Its Effect on the Exciton Dynamics of CdSe Quantum Dots. *J. Phys. Chem. C* **2012**, *116*, 13452-13457.

(51) May, M. M.; Lewerenz, H.-J.; Hannappel, T. Optical in Situ Study of InP(100) Surface Chemistry: Dissociative Adsorption of Water and Oxygen. *J. Phys. Chem. C* **2014**, *118*, 19032-19041.

(52) Hofmann, A.; Streubel, P.; Meisel, A. XPS investigation of oxide films on InP(100). *Surf. Interface Anal.* **1988**, *12*, 315-319.

(53) Kohl, P. A.; Wolowodiuk, C.; Ostermayer, F. W. The Photoelectrochemical Oxidation of (100), (111), and ($\bar{1}\bar{1}\bar{1}$) n - InP and n - GaAs. *J. Electrochem. Soc.* **1983**, *130*, 2288.

(54) Koppenol, W. H.; Stanbury, D. M.; Bounds, P. L. Electrode potentials of partially reduced oxygen species, from dioxygen to water. *Free Radical Biol. Med.* **2010**, *49* (3), 317-322. DOI: https://doi.org/10.1016/j.freeradbiomed.2010.04.011.

(55) Aldana, J.; Wang, Y. A.; Peng, X. Photochemical Instability of CdSe Nanocrystals Coated by Hydrophilic Thiols. *J. Am. Chem. Soc*. **2001**, *123*, 8844-8850.

(56) Caputo, J. A.; Frenette, L. C.; Zhao, N.; Sowers, K. L.; Krauss, T. D.; Weix, D. J. General and Efficient C–C Bond Forming Photoredox Catalysis with Semiconductor Quantum Dots. *J. Am. Chem. Soc*. **2017**, *139*, 4250-4253.

(57) Huang, Z.; Guan, R.; Shanmugam, M.; Bennett, E. L.; Robertson, C. M.; Brookfield, A.; McInnes, E. J. L.; Xiao, J. Oxidative Cleavage of Alkenes by O_2 with a Non-Heme Manganese Catalyst. *J. Am. Chem. Soc*. **2021**, *143*, 10005-10013.

Table of Contents